International Journal of Hydrogen Energy 90 (2024) 246–256

Contents lists available at ScienceDirect

International Journal of Hydrogen Energy

journal homepage: www.elsevier.com/locate/he

Hydrogen and vacancy concentrations in α-iron under high hydrogen gas pressure and external stress: A first-principles neural network simulation study

Shihao Zhang[1], Shihao Zhu[1], Fanshun Meng, Shigenobu Ogata *

Department of Mechanical Science and Bioengineering, Graduate School of Engineering Science, Osaka University, Osaka, 560-8531, Japan

ARTICLE INFO

Keywords:
Iron
Hydrogen solubility
Sieverts' law
Chemical potential
Vacancy formation free energy
First-principles neural network potential

ABSTRACT

The metal-hydrogen-vacancy interaction in α-iron is crucial for understanding hydrogen embrittlement behavior and developing reliable materials for green gaseous hydrogen applications; however, it remains underexplored, particularly in contexts involving external stress and high hydrogen gas pressure. In this study, we performed quantitative analyses of metal-vacancy–hydrogen interactions in α-iron, measured by hydrogen solubility and the thermodynamics of vacancy–hydrogen complexes, under such challenging conditions using a reliable first-principles neural network potential. High hydrogen gas pressures reaching up to 2 GPa were investigated. As the atomic concentration surpasses approximately 0.01, hydrogen solubility is dominated by hydrogen-induced lattice distortion (primarily volumetric expansion) and the interactions between hydrogen atoms within the metal matrix, resulting in significant deviations from Sieverts' law. Our results reveal a significant effect of shear stress on hydrogen solubility, deviating from previously used equations. Moreover, the influence of external stress on the thermodynamics of the vacancy–hydrogen complex, particularly vacancy formation free energy, is uniquely characterized by hydrogen solubility, regardless of the external stress magnitude. It thereby offers a rapid method to estimate the vacancy properties under external stress based on readily accessible external-stress-free data.

1. Introduction

Green gaseous hydrogen is one of the most promising energy carriers in the near future [1–3], necessitating the compression or liquefaction of the gas under high pressure to increase the volumetric energy density to a practical level. One of the challenges is establishing reliable and safe structures for transmission and storage, such as pipelines and pressure vessels. It is because high-strength steel typically suffers from a loss in ductility due to hydrogen dissolution when exposed to high-pressure hydrogen gas, a phenomenon known as hydrogen embrittlement (HE) [4–6]. Dissolved hydrogen atoms interact with tensile stress fields at the crack tip and other defects [7,8], in addition to the reactive chemical field at the defects, which can be significant, locally increasing the hydrogen content and facilitating the effects of hydrogen on deformation and fracture processes [7,8]. Assuming an ideal solution, the equilibrium hydrogen concentration c_H depends solely on the pressure of H_2 in an ideal gas, i.e.,

$$c_H = K P^{1/2} \tag{1}$$

where K is the temperature-dependent coefficient. At high pressures, P should be replaced by the fugacity f of hydrogen gas. Eq. (1), known as Sieverts' law [9], is applicable under conditions of low concentration. This law does not consider interactions between hydrogen atoms within the iron matrix, thus deviations are anticipated at elevated high concentrations and high hydrogen pressure. At these levels, the reduction in inter-atomic distances renders such interactions significant. Therefore, understanding the "real" solubility of high-pressure hydrogen gas and the hydrogen–hydrogen interactions within the metal matrix at high concentrations becomes essential.

Vacancies can be stabilized in a hydrogen environment owing to the vacancy–hydrogen interaction, leading to the formation of vacancy–hydrogen complexes and thereby increasing the vacancy concentration in metals [10]. This phenomenon contributes to hydrogen embrittlement via void formation resulting from vacancy clustering [11,12]. Consequently, it is critical to determine the extent to which hydrogen stabilizes vacancies. Understanding how this stabilization depends on hydrogen gas pressure and temperature is also essential.

* Corresponding author.
E-mail address: ogata@me.es.osaka-u.ac.jp (S. Ogata).
[1] These authors contributed equally to this work.

https://doi.org/10.1016/j.ijhydene.2024.09.378
Received 18 July 2024; Received in revised form 5 September 2024; Accepted 26 September 2024
Available online 4 October 2024

The significant stress fields near crack tips and dislocations, which are directly associated with hydrogen embrittlement behavior, underscore the importance of clarifying the external stress's influence on this stabilization. Overall, for comprehending HE behavior and developing reliable materials for green gaseous hydrogen applications, understanding the metal-hydrogen-vacancy interaction becomes crucial, especially under conditions of external stress and high hydrogen gas pressure, including hydrogen solubility and thermodynamics of vacancy–hydrogen complex. However, experimental reports on these aspects are sparse due to technical challenges. For instance, so far, there has been no experimental report on hydrogen solubility with hydrogen gas pressure larger than 100 MPa [13].

In this work, we conducted molecular dynamics simulations to estimate the metal-hydrogen-vacancy interaction in α-iron via the hydrogen solubility varying with temperature and external stress under high hydrogen gas pressures up to 2 GPa, as well as the vacancy formation free energy and vacancy concentration dependent on hydrogen gas pressure and external stress under the same conditions. It is important to note that hydrogen storage containers typically do not operate at GPa-level pressures due to the minimal volumetric benefit at pressures above tens of MPa, as well as challenges related to material strength. However, in this work, hydrogen solubility at high pressures, up to 2 GPa, was investigated for the following reasons: (1) GPa-level pressure is pertinent in conditions such as acid or electrical charging [14,15], as well as in certain material fracture mechanics testing platforms using high-pressure hydrogen [16]; (2) Understanding hydrogen solubility at high concentrations, corresponding to high pressures, is crucial for assessing areas of high-stress concentration that locally increase hydrogen levels. This is essential for addressing hydrogen embrittlement and advancing applications in hydrogen energy. These simulations employed our first-principles neural network interatomic potential for the iron/hydrogen binary system [8,17]. We found that at atomic concentrations exceeding approximately 0.01, solubility is affected by hydrogen-induced lattice distortion (primarily volumetric expansion) and the interactions between hydrogen atoms within the metal matrix, resulting in significant deviations from Sieverts' law. Our research reveals the significant effect of shear stress on hydrogen solubility, deviating from previously used equations. It is pivotal for understanding hydrogen behavior in structural materials, especially in stress–concentration contexts. Furthermore, the role of external stress on the thermodynamics of the vacancy–hydrogen complex, particularly in formulating vacancy free energy, is uniquely determined by hydrogen solubility, regardless of the external stress magnitude. It thus offers a rapid method to estimate vacancy properties under external stress using readily available external-stress-free data.

2. Theory and method

In this study, we employed two simulation methods to determine the solubility of hydrogen under various hydrogen gas pressures and temperatures in α-iron, as illustrated in Fig. 1a. The first method utilized a hybrid approach that combines molecular dynamics (MD) and Grand Canonical Monte Carlo (GCMC) simulations [18] (detailed in Section 2.1). This method allowed us to link the chemical potential of interstitial hydrogen atoms in iron, $\mu_{\mathrm{H,sol}}$, with the hydrogen concentration, c_{H}. By integrating the relationships between the pressure P and fugacity f of hydrogen gas (refer to Section 2.2 and Eq. (4)), as well as between f and $\mu_{\mathrm{H,sol}}$ (see Section 2.3 and Eq. (8)), we derived a relationship between the hydrogen concentration c_{H} and the gas pressure P. Here, a straightforward MD simulation was performed to establish the P–f relationship for hydrogen gas. The second method involved direct hydrogen gas charging MD simulations on an α-iron slab model until the chemical potentials of hydrogen gas and the hydrogen atom in iron matrix are balanced. This approach not only directly determined the relationship between c_{H} and P but also defined a fugacity parameter in the fugacity–chemical potential relationship (detailed in Section 2.4).

2.1. Hybrid MD/GCMC simulation

The concentration of hydrogen (c_{H}) was determined as a function of the chemical potential of solvated hydrogen ($\mu_{\mathrm{H,sol}}$) using a hybrid MD/GCMC simulation [18], specifically within the NVT (MD) and μVT (GCMC) ensembles. This setup facilitated the insertion and deletion of hydrogen atoms at a fixed chemical potential, as illustrated in Fig. 1b. MD simulations were conducted with a constant time step of 0.5 fs, and every 10 MD steps were followed by 100 GCMC trials. To achieve the desired external stress, the size of the supercell was adjusted dynamically to maintain an average pressure within the simulation cell.

All simulations were conducted using the Large-scale Atomic/Molecular Massively Parallel Simulator (LAMMPS) code [19], paired with our previously developed first-principles neural network interatomic potential for the iron/hydrogen binary system [8,17]. This potential provides accuracy comparable to first-principles calculations but at a lower computational cost. For comprehensive details on the training dataset and validation results, please refer to our prior publications [8,17].

2.2. Fugacity of hydrogen gas

The thermodynamics of real gases can be rigorously addressed with the understanding of the fugacity f. The concept of fugacity f is introduced in a form analogous to that of the ideal case, i.e.,

$$(d\mu)_T = RT(d\ln f)_T \tag{2}$$

compared to $(d\mu)_T = RT(d\ln P)_T$ for an ideal gas. By combining them with the chemical potential expression of any system $(d\mu/dP)_T = V_m$ and the ideal gas law $(d\mu/dP)_T = V_m^0 = RT/P$, the fugacity can be related to the equation of state and the properties of the ideal gas as

$$\ln\frac{f}{f_0} - \ln\frac{P}{P_0} = \frac{1}{RT}\int_{P_0}^{P}\left(V_m - V_m^0\right)dP \tag{3}$$

Using the limiting behavior of fugacity ($f_0 \to P_0$, when $P_0 \to 0$), the fugacity can be expressed in the following form [20,21]:

$$\ln\frac{f}{P} = \int_0^P\left(\frac{V_m}{RT} - \frac{1}{P}\right)dP \tag{4}$$

where P and T represent the gas pressure and absolute temperature of the system, respectively; P_0 is the gas pressure and f_0 is the fugacity at the reference state; and V_m is the molar volume of hydrogen molecules while V_m^0 are that in the ideal case. R is the universal gas constant.

The molar volume of hydrogen molecules V_m, as a function of P and T, was calculated directly through MD simulations. A total of 600 hydrogen molecules were placed in a simulation cell measuring 3 nm × 3 nm × 3 nm, configured with an NPT ensemble and periodic boundaries in all directions (see Fig. 1c). A time step of 0.5 fs was used throughout the simulations. Equal pressure was applied to all three cell dimensions. V_m was subsequently derived from the equilibrium volume of the simulation cell, averaged over 0.5 ns after a 1.0 ns equilibrium period. $V_m(P,T)$ was then substituted into Eq. (4) to determine the fugacity of hydrogen gas for a given set of conditions (P,T).

2.3. Thermodynamics of hydrogen molecule dissolution

The dissolution of $x/2$ hydrogen gas molecules H_2 by iron can be described by the reaction: $Fe + (x/2)H_2 \to FeH_x + x\Delta H$, where ΔH is the enthalpy of solution, representing the heat released per absorbed hydrogen atom. The thermodynamic equilibrium for the reaction requires

$$\frac{1}{2}\mu_{\mathrm{H_2,gas}} = \mu_{\mathrm{H,sol}}(c_{\mathrm{H}}) \tag{5}$$

where $\mu_{\mathrm{H_2,gas}}$ is the chemical potential of hydrogen gas, $\mu_{\mathrm{H,sol}}$ is the chemical potential of hydrogen atoms interstitial in iron, c_{H} is the hydrogen concentration in iron, and the factor 1/2 accounts for the

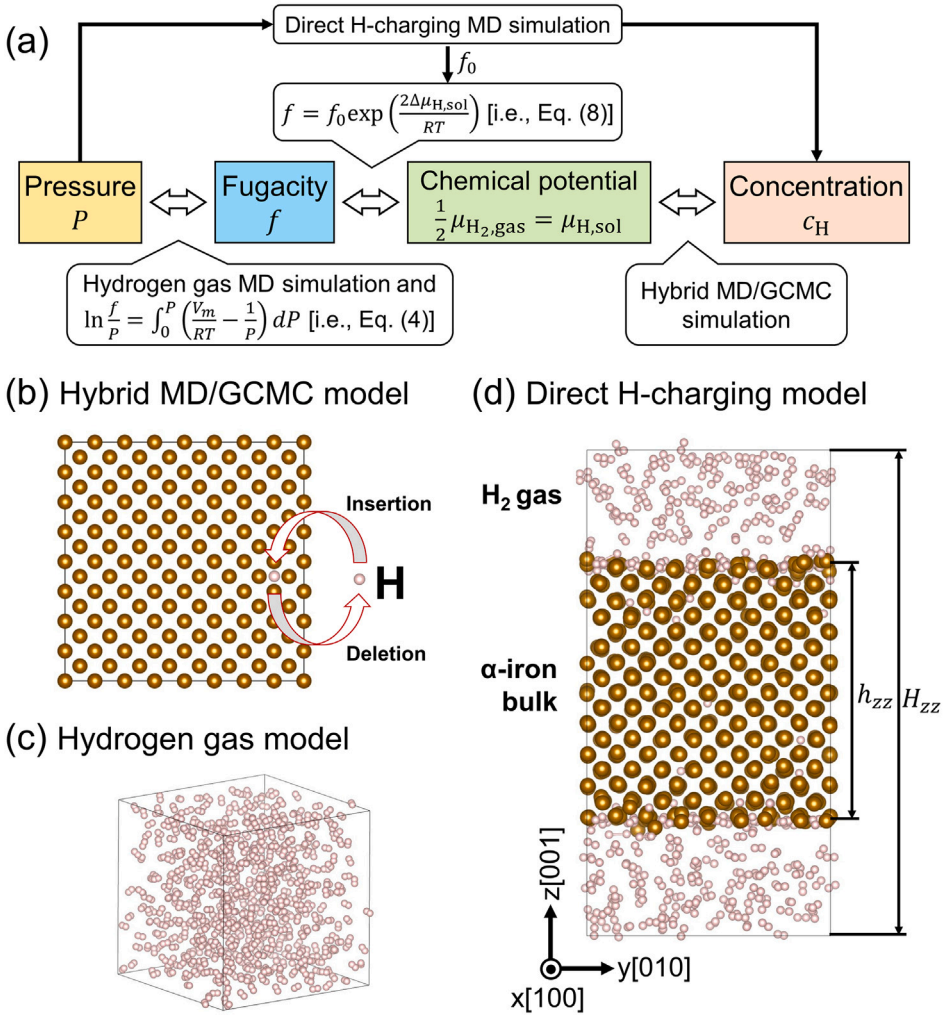

Fig. 1. (a) The workflow of this work to determine the high-pressure hydrogen solubility, where P and f are the pressure and fugacity of hydrogen gas, $\mu_{H_2,gas}$ and $\mu_{H,sol}$ are the chemical potentials of the hydrogen gas and the interstitial hydrogen atoms in iron, and c_H is the hydrogen concentration, respectively. (b-d) The schematic drawing of MD simulation settings for (b) the hybrid MD/GCMC model, which allows for the insertion and deletion of hydrogen atoms at a fixed chemical potential, (c) the hydrogen gas model used to calculate the fugacity, and (d) the direct H-charging model used to perform the direct H-charging MD simulation of gas solubility.

fact that a hydrogen molecule consists of two hydrogen atoms. Taking $\mu^0_{H,sol} = \mu_{H,sol}(c^0_H)$ as a reference state, which reaches thermodynamic equilibrium with the hydrogen gas with chemical potential $\mu^0_{H_2,gas}$ and fugacity f_0, Eq. (5) can be expressed as

$$\frac{1}{2}\left(\mu^0_{H_2,gas} + RT\ln\frac{f}{f_0}\right) = \mu^0_{H,sol} + \Delta\mu_{H,sol} \tag{6}$$

where $(1/2)\mu^0_{H_2,gas} = \mu^0_{H,sol}$, and c^0_H is the hydrogen concentration in iron at the reference state. Therefore,

$$\frac{1}{2}RT\ln\frac{f}{f_0} = \Delta\mu_{H,sol} \tag{7}$$

i.e.,

$$f = f_0 \exp\left(\frac{2\Delta\mu_{H,sol}}{RT}\right) \tag{8}$$

The prefactor f_0 in Eq. (8), corresponding to an equilibrium hydrogen concentration of c^0_H, was determined through a single MD simulation of direct hydrogen gas charging (refer to Section 2.4).

2.4. Direct hydrogen gas charging MD simulations on an α-iron slab model

For the direct H-charging MD simulation to determine the hydrogen gas solubility, an atomistic slab model of α-iron measuring 2.3 nm × 2.3 nm × 2.3 nm was constructed, consisting of 1088 iron atoms. The model's orientation was x: [100], y: [010], and z: [001] (see Fig. 1d). A total of 1000 hydrogen molecules were then introduced into the vacuum regions above and below the iron specimen, and the hydrogen gas pressure was controlled within the NPT ensemble. Periodic boundary conditions were applied in all three dimensions. A time step of 0.5 fs was used throughout the simulations. To mitigate the undesired expansion of the simulation cell in the x and y directions due to the influence of hydrogen gas pressure P in the z direction, we introduced a specified pressure component in the x and y directions:

$$P_{xx} = P_{yy} = \frac{H_{zz} - h_{zz}}{H_{zz}}P \tag{9}$$

where H_{zz} represents the length of the simulation cell along the z-axis, and h_{zz} is the thickness of the iron bulk in the z direction as illustrated in Fig. 1d; P_{xx} and P_{yy} are the pressure components of the entire simulation cell along x- and y-axes, respectively. This adjustment effectively eliminated the non-negligible stress effects, resulting from the expansion of the simulation cell, on the hydrogen solubility.

To ensure an accurate assessment of hydrogen solubility, we monitored the concentration of hydrogen atoms in the iron bulk region, excluding the outermost three layers of iron atoms in the slab model. Throughout the simulation, more than 3.0 ns was allotted for the system to reach equilibrium. Then, a time frame of 1.0 ns was used to calculate the equilibrium hydrogen concentration c_H with the given

pressure and temperature of hydrogen gas by averaging over the time interval. This approach effectively eliminated the impact of hydrogen near the iron surfaces.

2.5. Thermodynamics of vacancy–hydrogen complex in α-iron

Based on the definition of chemical potential [22], the effect of the trapped H atoms on the formation free-energy $\Delta G_f = G_f^{\mathrm{H}} - G_f^0$ of monovacancy can be determined as

$$\Delta G_f = -\int_{-\infty}^{\mu_{\mathrm{H,sol}}^*} \langle N \rangle d\mu_{\mathrm{H,sol}} \tag{10}$$

where G_f^{H} and G_f^0 are the formation free energy of H-trapped vacancy with $\mu_{\mathrm{H,sol}} = \mu_{\mathrm{H,sol}}^*$ and H-free vacancy with $\mu_{\mathrm{H,sol}} = -\infty$, respectively; $\langle N \rangle$ is the average number of the trapped H atoms at vacancy as a function of the $\mu_{\mathrm{H,sol}}$. The brackets $\langle\ \rangle$ means the ensemble average. Based on the general relationship $c_{\mathrm{vac}}^0 = \exp(-G_f^0/RT)$ and $c_{\mathrm{vac}}^{\mathrm{H}} = \exp(-G_f^{\mathrm{H}}/RT)$ in the dilute limit of vacancy concentration [23,24], the hydrogen-induced change of the equilibrium concentration of vacancy is given by

$$\frac{c_{\mathrm{vac}}^{\mathrm{H}}}{c_{\mathrm{vac}}^0} = \exp\left(-\frac{\Delta G_f}{RT}\right) \tag{11}$$

where $c_{\mathrm{vac}}^{\mathrm{H}}$ and c_{vac}^0 are the equilibrium concentration of vacancy in H-charged iron and H-free iron, respectively.

To determine the average number of hydrogen trapped at vacancy under an applied chemical potential $\mu_{\mathrm{H,sol}}$, the hybrid MD/GCMC simulations [18] were carried out. Every 10 MD steps, 100 GCMC trails were carried out, and hydrogen atoms were therefore inserted in and extracted from the sample. The size of the simulation model is $(8 \times 8 \times 8)$ a_0, where a_0 is the lattice constant of α-iron. The periodic boundary conditions were imposed in all three directions and a monovacancy was created in the model by removing an iron atom. The average number of hydrogen atoms trapped at vacancy was determined by averaging over 0.2 ns after 0.05 ns for equilibrium.

3. Fugacity of hydrogen gas

For conditions where the Abel-Noble (AN) equation of state [25] is appropriate, i.e., $V_m = RT/P + b$ and $V_m/RT - 1/P = b/RT$, fugacity can be expressed as a simple function of pressure and temperature by substituting the AN equation into Eq. (4):

$$f = P\exp\left(\frac{Pb}{RT}\right) \tag{12}$$

where b is a constant. With b = 15.84 cm^3 mol^{-1}, Eq. (12) has been demonstrated to agree well with the experimental value [21] with the pressure of hydrogen gas ranging from 5 to 300 MPa.

Fig. 2a shows the value of $V_m/RT - 1/P$ as a function of hydrogen gas pressure P. In the case of high gas pressure, the value of $V_m/RT - 1/P$ is no longer equal to a constant b/RT as predicted by the AN equation but decreases linearly as the gas pressure increases. Therefore, in this work, we modified the AN equation as:

$$\frac{V_m}{RT} - \frac{1}{P} = \frac{aP}{RT} + \frac{b}{RT} \tag{13}$$

where a and b are constants, determined by linearly fitting the $(V_m/RT - 1/P) - P$ curve shown in Fig. 2a. In this work, a and b were determined as −0.003118 cm^3 mol^{-1} MPa^{-1} and 16.26 cm^3 mol^{-1}, respectively. The determined value of b is very close to the experimental value of 15.84 cm^3 mol^{-1} [21]. Inserting the modified AN equation (i.e., Eq. (13)) into Eq. (4), Eq. (12) changes to

$$f = P\exp\left(\frac{P^2a}{2RT} + \frac{Pb}{RT}\right) \tag{14}$$

Fig. 2b presents the fugacity of hydrogen gas as a function of pressure determined directly through MD simulations. The relationship

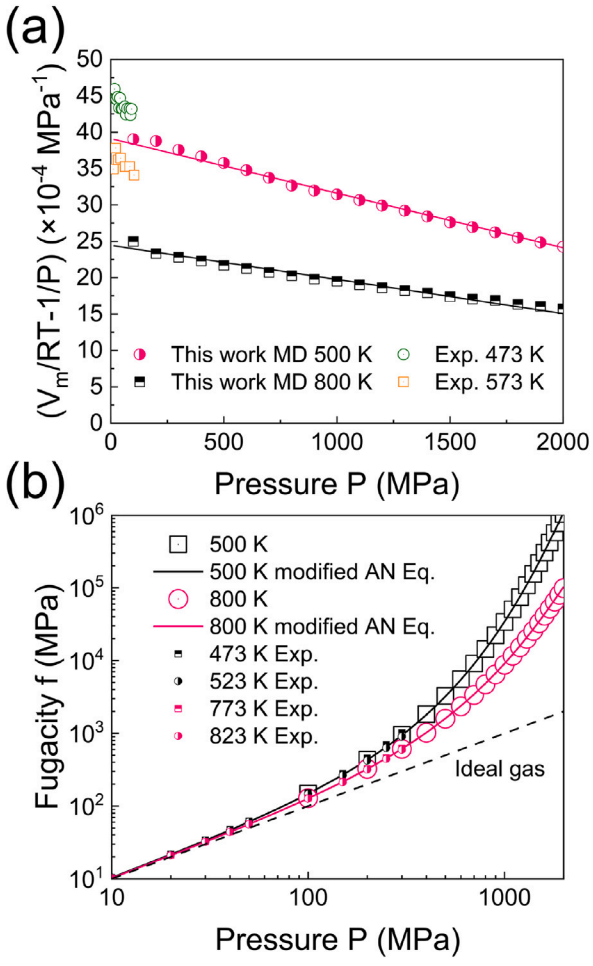

Fig. 2. (a) The relationship between $V_m/RT - 1/P$ and P. The lines show the linear fitting results. (b) Fugacity of hydrogen gas as a function of its pressure, as determined using the hydrogen gas model shown in Fig. 1c (represented by symbols), with the results computed via Eq. (14) (represented by lines), where a =-0.003118 cm^3 mol^{-1} MPa^{-1} and b = 15.84 cm^3 mol^{-1}. The experimental data [21] is also shown for comparison.

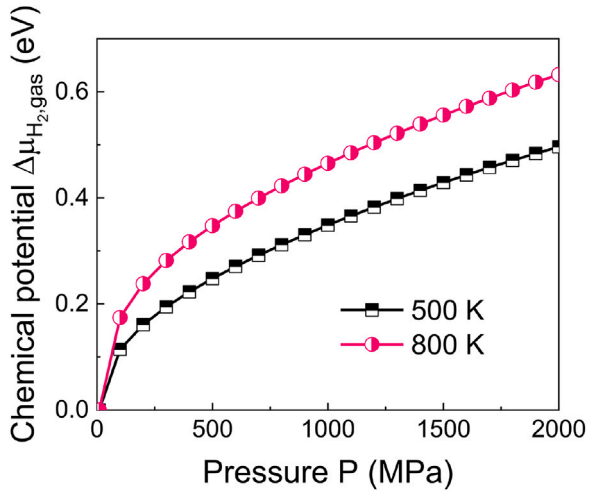

Fig. 3. The chemical potential of hydrogen gas $\Delta\mu_{\mathrm{H_2,gas}} = \mu_{\mathrm{H_2,gas}} - \mu_{\mathrm{H_2,gas}}^0 = RT\ln f/f_0$ as a function of hydrogen gas pressure P, taking the hydrogen gas with chemical potential $\mu_{\mathrm{H_2,gas}}^0$ and fugacity $f_0 \approx P$ = 10 MPa as a reference state.

between the fugacity and pressure of hydrogen gas adheres to the modified AN equation up to pressures of 2 GPa. To be noted that at a high pressure of 2 GPa, it is more appropriate to refer to hydrogen as being in a fluid state rather than as a gas [26]. By integrating both side of Eq. (2), we have the relationship $\mu_{H_2,gas} = \mu^0_{H_2,gas} + RT \ln f/f_0$, where $\mu^0_{H_2,gas}$ and f_0 are the chemical potential and fugacity of hydrogen gas at a reference stare. By inserting the results of f as a function of pressure P shown in Fig. 2b into the above equation, we can directly derive the relationship between the chemical potential and the pressure of hydrogen gas. The results are illustrated in Fig. 3.

4. Hydrogen solubility

Using Eq. (14) together with Eq. (8), we have the relationship between $\Delta\mu_{H,sol}$ and P as $P\exp\left(\frac{P^2 a}{2RT} + \frac{Pb}{RT}\right) = f_0 \exp\left(\frac{2\Delta\mu_{H,sol}}{RT}\right)$. Combining with the relationship between $\Delta\mu_{H,sol}$ and c_H, determined via the hybrid MD/GCMC simulation in this work, we illustrate the atomic concentration of hydrogen (c_H) as a function of the square root of hydrogen gas pressure ($P^{1/2}$) in Fig. 4a. Additionally, we plot experimental data on hydrogen solubility in super-pure iron single crystals at temperatures of 555 K and 794 K [27], providing context for our findings within established research. For hydrogen gas pressures less than approximately 4 MPa, c_H increases linearly with increasing $P^{1/2}$, thereby adhering to Sieverts' law (Eq. (1)). Linear fitting yielded constants (K values) of 0.36×10^{-4} and 6.3×10^{-4} $MPa^{-1/2}$ for temperatures of 500 K and 800 K, respectively. However, as P continues to increase, the relationship between c_H and $P^{1/2}$ deviates from linearity, indicating the "real" behavior of hydrogen gas measured by the fugacity f. As shown in Fig. 4b, c_H is linearly related to $f^{1/2}$ until reaching approximately 0.01 atomic concentration.

Upon exceeding a hydrogen atomic concentration (c_H) of 0.01, substantial hydrogen-induced volumetric expansion is observed. Fig. 5a demonstrates this expansion, showcasing a linear increase in the volume per iron atom as c_H rises, resulting in a partial molar volume of hydrogen V_H of 4.1 $Å^3$/atom. This value aligns with experimental values of 3.3, 2.0, 4.4, and 5.0 $Å^3$/atom reported in previous studies [28–31]. Due to this hydrogen-induced volumetric expansion, a steep rise in c_H is noted in Fig. 4, which is further depicted in Fig. 5b, illustrating the correlation between the volume per iron atom, c_H, and the square root of hydrogen gas pressure. This steep rise owing to hydrogen-induced volumetric expansion is further supported by results from our hybrid MD/GCMC simulations with a fixed model volume [17] shown in Fig. 4b, where the steep rise is absent.

Additionally, the c_H determined with a fixed model volume deviates from linearity with respect to $f^{1/2}$ as the atomic concentration surpasses 0.01. This suggests that hydrogen–hydrogen interactions within the iron matrix become pronounced, increasing the dissolution energy of hydrogen atoms in iron and thereby suppressing hydrogen solubility. As the concentration rises, the effect of hydrogen–hydrogen interactions on hydrogen solubility becomes dominant compared to the effect of hydrogen-induced volumetric expansion, creating a noticeable inflection point on the c_H–$f^{1/2}$ curve when $c_H \approx 0.08$, as shown in Fig. 4b. To be noted that under the hydrogen gas pressure up to 2 GPa, no hydride formation occurs because hydride formation in iron requires significantly higher pressures, e.g., 3.5 GPa at 298 K [32] and 6 GPa at 523 K [33].

In summary, the study into hydrogen solubility under high-pressure gas conditions, reaching up to 2 GPa with the aid of a neural network potential, unveils significant deviations from Sieverts' law once the atomic concentration surpasses 0.01. The corresponding pressures of hydrogen gas are approximately 960 MPa at 500 K and 130 MPa at 800 K under external-stress-free conditions in an iron matrix. The deviations are attributed to the hydrogen-induced volumetric expansion and hydrogen–hydrogen interactions within the iron matrix. These findings provide critical physical insights that are unattainable through traditional experimental and simulation approaches, such as the embedded atom method potential and density functional theory calculation, yet essential for advancing hydrogen energy engineering applications [16].

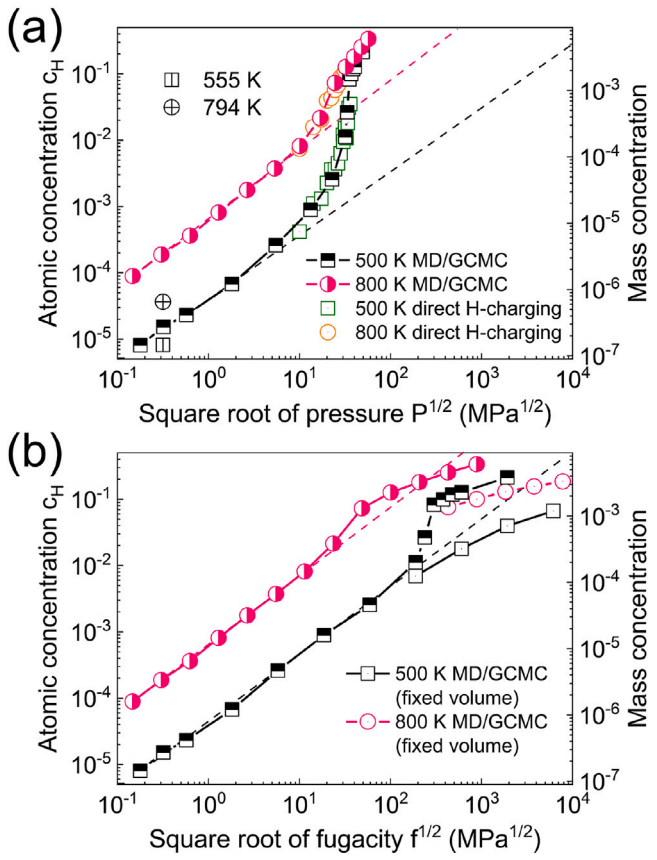

Fig. 4. Hydrogen atomic concentration (c_H) as a function of (a) the square root of hydrogen gas pressure $P^{1/2}$ and (b) the square root of hydrogen gas fugacity $f^{1/2}$, as determined through hybrid MD/GCMC simulation and direct H-charging MD simulation. The results of the hybrid MD/GCMC simulation with a fixed model volume [17] are also included for comparison. Experimental results of super-pure-iron single crystals at temperatures of 555 K and 794 K [27] are also shown for comparison. The corresponding mass concentrations of hydrogen are also shown.

5. Effect of external stress on hydrogen solubility

Based on the results discussed in the previous section regarding lattice strains induced by hydrogen charging, it is anticipated that hydrogen concentration will vary as a result of these strains and/or the associated external stresses. Such strains and external stresses may be imposed by mechanical loads applied externally to the material or may arise locally due to stress concentrations caused by lattice defects. In particular, stress intensification near crack tips and edge dislocations is expected to produce tensile stresses that significantly exceed those from the external load, thereby leading to a marked increase in local hydrogen concentration. This localized hydrogen distribution can promote defect evolution, such as crack propagation and dislocation activities, potentially enhancing HE.

We investigated the impact of various types of external stress on hydrogen solubility, including: (i) volumetric stress, (ii) uniaxial stress along [001], (iii) uniaxial stress along [011], (iv) uniaxial stress along [111], (v) shear stress in the (001)[100] direction, and (vi) shear stress in the $(1\bar{1}0)[111]$ direction. The stress conditions were defined in Voigt notation [34] as follows: (i) $\boldsymbol{\sigma}^{ex} = \{\sigma_1, \sigma_2, \sigma_3, \sigma_4, \sigma_5, \sigma_6\} = \{\sigma/3, \sigma/3, \sigma/3, 0, 0, 0\}$, (ii) $\boldsymbol{\sigma}^{ex} = \{0, 0, \sigma, 0, 0, 0\}$, (iii) $\boldsymbol{\sigma}^{ex} = \{0, \sigma/2, \sigma/2, \sigma/2, 0, 0\}$, (iv) $\boldsymbol{\sigma}^{ex} = \{\sigma/3, \sigma/3, \sigma/3, \sigma/3, \sigma/3, \sigma/3\}$, (v) $\boldsymbol{\sigma}^{ex} = \{0, 0, 0, \sigma, 0, 0\}$, and (vi) $\boldsymbol{\sigma}^{ex} = \{(\sqrt{6}/3)\sigma, -(\sqrt{6}/3)\sigma, 0, -(\sqrt{6}/6)\sigma, (\sqrt{6}/6)\sigma, 0\}$, within the coordinate frame of x[001], y[010], and z[001], respectively, where σ is the stress value. For the volumetric stress and the uniaxial stresses along [001], [011], and [111], the value of

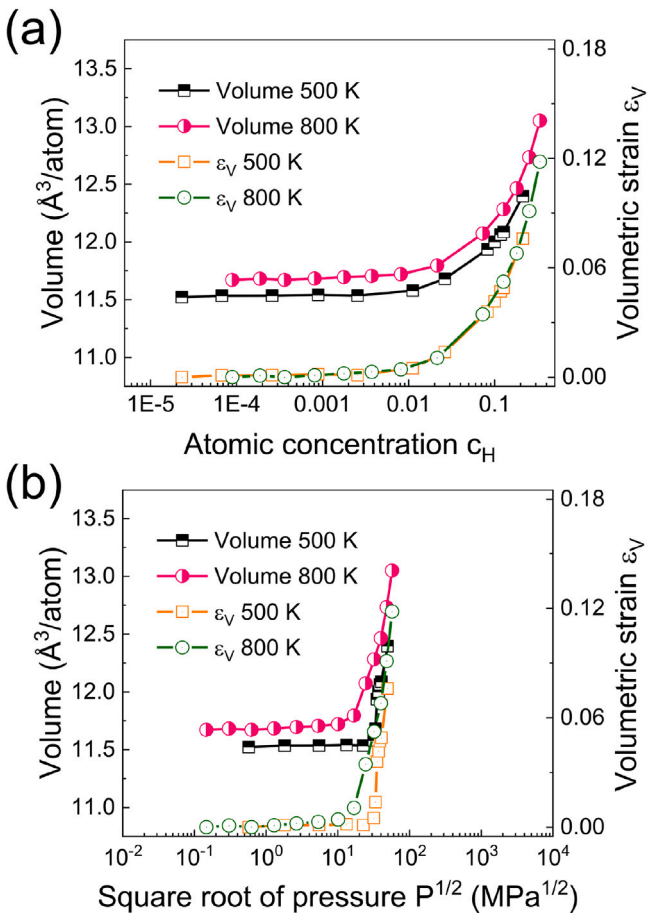

Fig. 5. Relationships of the volume per iron atom and volumetric strain $\varepsilon_V = (\Omega_H - \Omega_0)/\Omega_0$ with (a) the hydrogen atomic concentration c_H and (b) the corresponding square root of hydrogen gas pressure $P^{1/2}$. Ω_H and Ω_0 are the volumes per iron atom of H-charging and H-free samples, respectively. It is important to note that the dissolution of hydrogen does not induce shear strain, i.e., $\varepsilon_{xy} = \varepsilon_{yz} = \varepsilon_{xz} = 0$.

$\bar{\sigma} = \sigma_{ii}/3$ (i.e., 1/3 of the trace of the stress tensor $\boldsymbol{\sigma}$) remains the same and is equal to $\sigma/3$, albeit with different shear components. Conversely, for the shear stresses in the (001)[100] and $(1\bar{1}0)[111]$ directions, the value of $\bar{\sigma} = 0$.

The hydrogen atomic concentration (c_H) as a function of external stress σ is depicted in Figs. 6a–b. The results, determined using the following equation, are also presented:

$$\frac{c_H^{\sigma}}{c_H} = \exp\left(\frac{V_H \bar{\sigma}}{RT}\right) \tag{15}$$

which has been widely used to characterize the effect of external stress on hydrogen solubility [35,36]. Here, c_H represents the hydrogen concentration in the unstressed lattice, and c_H^{σ} denotes the concentration in the lattice under external stress $\bar{\sigma} = \sigma_{ii}/3$ (i.e., one-third of the trace of the stress tensor $\boldsymbol{\sigma}$); V_H is the partial molar volume of hydrogen in the lattice and was determined to be 4.1 Å^3/atom by linearly fitting the external-stress-free results under 500 K and 800 K shown in Fig. 5a. As illustrated in Fig. 7, the value of V_H remains nearly unchanged under stress compared to its external-stress-free value (i.e., 4.1 Å^3/atom).

For compressive stress up to −6 GPa, the effects of the volumetric stress and the uniaxial stresses along [001], [011], and [111] can be effectively described by Eq. (15). However, in the case of tensile stress, the effect of these external stresses is different, which follows the order: $\sigma_{[001]} > \sigma_{[011]} \approx \sigma_{[111]} > \sigma_V$. The effect is more significant than that predicted by Eq. (15). For instance, under a tensile stress of 5 GPa, $c_H^{\sigma_{[001]}}/c_H \approx 55$ and $c_H^{\sigma_V}/c_H \approx 9.5$. These values are much larger than those predicted by Eq. (15), i.e., $c_H^{\sigma}/c_H \approx 2.7$. In comparison, shear stress shows a slight effect on hydrogen solubility with the shear stress less than approximately 4 GPa, but under higher shear stress, the effect is comparable to that of tensile stress. The $(1\bar{1}0)[111]$ shear stress has a greater effect on hydrogen solubility than the (001)[100] shear stress. These results are significantly different from those predicted by Eq. (15), in which the (001)[100] and $(1\bar{1}0)[111]$ shear stresses should have negligible effect where $\bar{\sigma} = 0$. The varying effects of volumetric stress and uniaxial stresses along [001], [011], and [111], which share the same value of $\bar{\sigma} = \sigma_{ii}/3 = \sigma/3$, coupled with the significant impact of high (001)[100] and $(1\bar{1}0)[111]$ shear stresses where $\bar{\sigma} = 0$, suggest that the effect of external stress on hydrogen solubility is related not only to tensile components but also to shear components.

Aligning with the fact that hydrogen macroscopically induces volumetric expansion in iron, the effect of external stress on hydrogen solubility is due to its impact on the volume of the iron matrix. Tensile stress increases the volume of the iron matrix, thereby providing additional space for hydrogen dissolution. Therefore, different types of external stress, leading to varying degrees of volume change, subsequently affect the solubility of hydrogen in various ways. Figs. 6c–d shows the results of $\Delta\Omega$ induced by external stress. The crystalline anisotropy results in variability in the value of $\Delta\Omega$ for different external stresses. The [001] uniaxial tensile stress results in the largest $\Delta\Omega$ compared to those of other types of external stress under the same value of σ. Therefore, it leads to the most significant increase in hydrogen solubility. The (001)[100] and $(1\bar{1}0)[111]$ shear stresses also cause noticeable volume expansion under high shear stress, resulting in a comparable effect on hydrogen solubility to that of tensile external stress.

The stress fields surrounding four typical defects in α-iron are illustrated in Fig. S1 in the Supplementary, including vacancy-type and interstitial-type dislocation loops [37–40], screw straight dislocation [41,42], and crack tip [7,43,44]. The stress fields surrounding these defects exceed 2 GPa in a region spanning tens of angstroms and can reach up to 6 GPa. Therefore, the external stress surrounding defects significantly affects localized hydrogen solubility. Specifically, for the crack tips, the high tensile stress level causes hydrogen atoms to preferentially be trapped at the crack tip. The aggregation of hydrogen can lead to brittle-cleavage failure followed by crack growth, resulting in a ductile-to-brittle transition [8].

Overall, these results highlight how the shear stress component significantly influences hydrogen solubility. There is a marked deviation of the effects of external stress from the predictions of the widely-used Eq. (15). The effect of shear stress on hydrogen solubility has been explored in previous studies [45,46], where the effects of shear strain on hydrogen solution energy in iron were investigated using first-principles calculations. In our study, we extend this understanding by exploring how various types of shear stresses affect hydrogen solubility, utilizing direct computations through our neural network potential. This insight is pivotal in elevating the understanding of the behavior of hydrogen in structural materials. It acquires a unique significance in scenarios marked by the concentrations of shear stress, such as screw dislocations, as reaffirmed by our emphasis on the considerable importance of the shear stress component.

As discussed in Section 4, when $c_H > 0.01$, both hydrogen-induced volumetric expansion and hydrogen–hydrogen interaction significantly affect hydrogen solubility. It is typically difficult for the hydrogen atomic concentration to reach 0.01 due to the high corresponding hydrogen gas pressure, especially at low temperatures. However, with the aid of stress acting on the iron lattice, the corresponding gas pressure can be significantly reduced. In regions with large stress fields, such as at a crack tip, the localized hydrogen atomic concentration could reach 0.01 even under low hydrogen gas pressures, which typically dominates the mechanism of HE. Therefore, it is crucial to consider the non-ideality in hydrogen solubility induced by hydrogen-induced

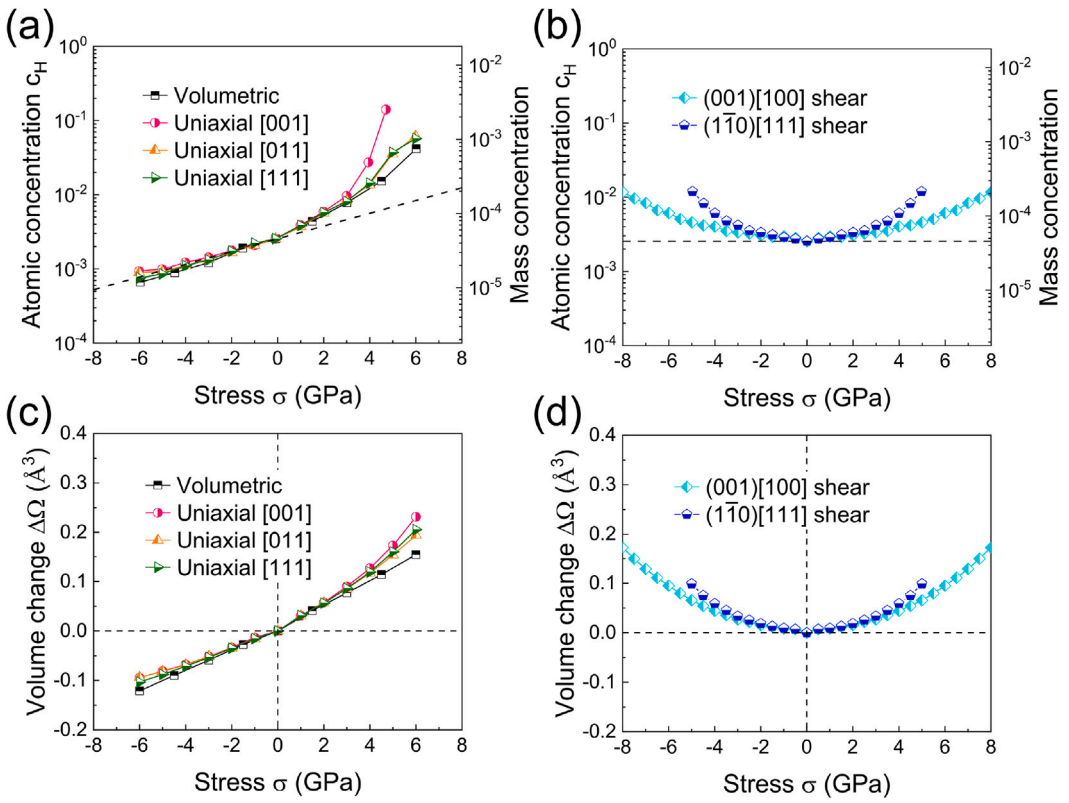

Fig. 6. The hydrogen atomic concentration (c_H) as a function of stress σ under various conditions: (a) volumetric stress, uniaxial [001], [011] and [111] stresses, and (b) (001)[100] and (1$\bar{1}$0)[111] shear stresses. The scenario is depicted with a chemical potential $\mu_{H,sol} = -2.3$ eV, corresponding to an unstressed hydrogen concentration of 2550 atomic ppm at 500 K. The results calculated via Eq. (15) are represented by a black dashed line, where $\bar{\sigma} = \sigma/3$ for (a) and $\bar{\sigma} = 0$ for (b). The volume change per atom $\Delta\Omega$ of H-free sample as a function of stress σ under various stress conditions: (c) volumetric stress, uniaxial [001], [011] and [111] stresses, and (d) (001)[100] and (1$\bar{1}$0)[111] shear stresses. The corresponding mass concentrations of hydrogen are also shown in (a–b).

volumetric expansion and hydrogen–hydrogen interaction to reveal the atomic mechanisms of HE in iron and steel.

It is important to note that, apart from stress fields generated by defects, hydrogen–defect chemical interactions can also attract more hydrogen to the defects, such as monovacancies, surfaces, grain boundaries, and dislocation cores. These interactions can alter the thermodynamic and kinetic properties of the defects, further enhancing HE. In the next section, we will discuss how monovacancy–hydrogen chemical interactions, through the formation of monovacancy–hydrogen complexes, lead to monovacancy stabilization.

6. Effect of external stress on the thermodynamics of vacancy–hydrogen complex

The interaction between monovacancies and hydrogen is critical because it is well-documented that monovacancies can trap hydrogen and become stabilized, even in the absence of external pressure [10]. The number of hydrogen atoms trapped by a monovacancy and the extent of monovacancy stabilization depends on variables such as hydrogen gas pressure (or hydrogen chemical potential), temperature, and external stress. Here, we demonstrate these relationships.

The average number $\langle N \rangle$ of hydrogen atoms trapped at monovacancy at 500 K and the resulting difference in the formation free energy of the vacancy ΔG_f as a function of external stress σ are shown in Fig. 8. Under the volumetric stress and uniaxial [001], [011] and [111] stresses, the $\langle N \rangle$ increases linearly from 3.2 to 4.2 with the value of σ increasing from −6 GPa to 6 GPa as shown in Fig. 8a. As a result, the formation free energy difference ΔG_f decreases linearly from −0.58 eV to −0.83 eV (see Fig. 8c); the vacancy concentration change c^H_{vac}/c^0_{vac}, determined using the ΔG_f (i.e., Eq. (11)), increases from 6.4×10^5 to 2.4×10^8 (see Fig. 8e). In comparison, (001)[100] and (1$\bar{1}$0)[111] shear stress shows little effect on the thermodynamics of vacancy–hydrogen complex, and the values of $\langle N \rangle$ and ΔG_f almost keep as a constant with the increasing value of the external shear stress as shown in Figs. 8b, d, and f.

In addition, Fig. 9 shows the $\langle N \rangle$ and ΔG_f as a function of hydrogen atomic concentration c_H with a variable of the external volumetric stress and uniaxial [001], [011] and [111] stresses with a constant $\mu_{H,sol} = -2.3$ eV. The $\langle N \rangle$ and ΔG_f, resulting from variations in the chemical potential $\mu_{H,sol}$ without external stress, are also plotted for comparison. Given the same c_H, the values of $\langle N \rangle$ and ΔG_f for the vacancy–hydrogen complex in both stressed and unstressed α-iron are nearly identical. It indicates that the influence of external stress on the values of $\langle N \rangle$ and ΔG_f for the vacancy–hydrogen complex is uniquely described by the hydrogen solubility, regardless of the external stress magnitude. Thereby, this finding suggests a pathway to quickly estimate the vacancy properties under external stress based on readily accessible external-stress-free data.

7. Summary

In the present study, we carried out assessments of the metal-hydrogen-vacancy interaction via hydrogen solubility and thermodynamics of the vacancy–hydrogen complex with high gas pressures up to 2 GPa. These assessments were performed through molecular dynamics simulations and a first-principles neural network interatomic potential of the binary system of iron/hydrogen. Our research reveals that when the atomic concentration of hydrogen surpasses roughly 0.01, hydrogen solubility is impacted by the volumetric expansion induced by hydrogen and the interactions between hydrogen atoms in

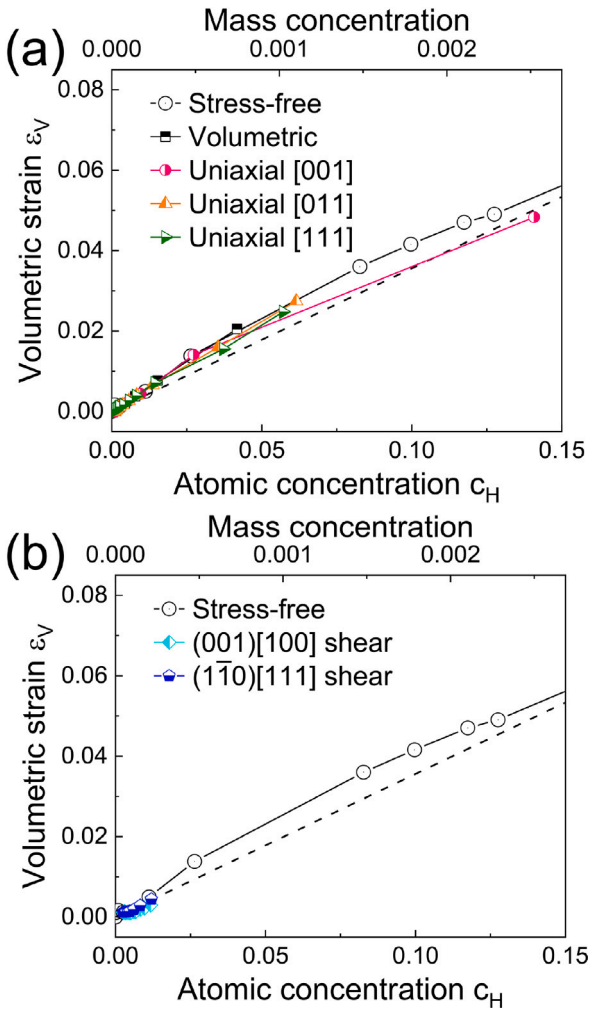

Fig. 7. Hydrogen charging induced volumetric strain $\varepsilon_V = (\Omega_H^\sigma - \Omega_0^\sigma)/\Omega_0^\sigma$ as a function of the hydrogen atomic concentration c_H under various stress conditions at 500 K: (a) volumetric stress, uniaxial [001], [011] and [111] stresses, and (b) (001)[100] and (1$\bar{1}$0)[111] shear stresses. Ω_H^σ and Ω_0^σ are the volumes per iron atom of H-charging and H-free samples under stress σ, respectively. The black dashed lines show the results calculated with $V_H = 4.1$ Å^3/atom, which was determined by linearly fitting the external-stress-free results under 500 K and 800 K shown in Fig. 5a. The corresponding mass concentrations of hydrogen are also shown.

the metal matrix, causing a significant departure from Sieverts' law. Our research reveals a significant effect of shear stress on hydrogen solubility, deviating from previously used equations. It is pivotal for understanding hydrogen behavior in structural materials, especially in stress–concentration contexts. Furthermore, the role of external stress on the thermodynamics of the vacancy–hydrogen complex, particularly in formulating vacancy free energy, is uniquely determined by hydrogen solubility, regardless of the strength of the external stress. It thus offers a rapid method to estimate vacancy properties under external stress using readily available external-stress-free data.

CRediT authorship contribution statement

Shihao Zhang: Writing – original draft, Visualization, Methodology, Investigation. **Shihao Zhu:** Writing – review & editing, Methodology, Investigation. **Fanshun Meng:** Writing – review & editing, Methodology. **Shigenobu Ogata:** Writing – review & editing, Supervision, Funding acquisition, Conceptualization.

Declaration of competing interest

The authors declare that they have no known competing financial interests or personal relationships that could have appeared to influence the work reported in this paper.

Acknowledgments

S.H.Z. and S.O. were funded by the JSPS Postdoctoral Fellowships for Research in Japan (Standard), the Grant -in-Aid for JSPS Research Fellow Grant No. 22F22056, and the JSPS KAKENHI Grant No. JP22KF0241. Part of the calculations were performed on the large-scale computer systems at the Cybermedia Center, Osaka University, the Large-scale parallel computing server at the Center for Computational Materials Science, Institute for Materials Research, Tohoku University, Research Center for Computational Science, Okazaki, Japan (Project: 24-IMS-C503), and supercomputer Fugaku provided by the RIKEN Center for Computational Science (Project IDs: hp230205 and hp230212). S.O. acknowledges the support by the Ministry of Education, Culture, Sport, Science and Technology of Japan (Grant Nos. JPMXP1122684766, JPMXP1020230325, and JPMXP1020230327), and the support by JSPS KAKENHI (Grant Nos. JP23H00161 and JP23K20037).

Appendix A

List of symbols used in this article as well as the calculated parameters in this work. f: fugacity.
P: pressure.
P_0: pressure for the reference state.
f: fugacity.
f_0: fugacity for the reference state.
R: universal gas constant.
T: temperature.
V_m: molar volume of hydrogen molecules.
V_m^0: molar volume of hydrogen molecules in the ideal case.
μ: chemical potential.
$\mu_{H,sol}$: chemical potential of hydrogen atoms interstitial in iron.
$\mu_{H_2,sol}$: chemical potential of hydrogen gas.
$\mu^0_{H,sol}$: chemical potential of hydrogen atoms interstitial in iron for the reference state.
$\mu^0_{H_2,sol}$: chemical potential of hydrogen gas for the reference state.
c_H: equilibrium concentration of hydrogen within the iron matrix.
c_H^0: equilibrium concentration of hydrogen within the iron matrix for the reference state.
$\langle N \rangle$: average number of the trapped hydrogen atoms at vacancy.
G_f^H and G_f^0: formation free-energy of H-charged and H-free vacancy, respectively.
ΔG_f: the change of the formation free-energy of vacancy owing to the trapping of H atoms at vacancy, i.e., $\Delta G_f = G_f^H - G_f^0$.
c_{vac}^H and c_{vac}^0: equilibrium concentration of vacancy in H-charged iron and H-free iron, respectively.
c_H^σ: equilibrium concentration of hydrogen within the iron matrix under external stress.
V_H: partial molar volume of hydrogen in the iron lattice, 4.1 Å^3/atom determined in this work.
σ: value of the external stress.
$\bar{\sigma}$: 1/3 of the trace of the external stress tensor $\boldsymbol{\sigma}$.
Ω: volume per iron atom.
a: −0.003118 cm^3 mol^{-1} MPa^{-1} in Eq. (13).
b: 16.26 cm^3 mol^{-1} in Eq. (13).

Appendix B. Supplementary data

Supplementary material related to this article can be found online at https://doi.org/10.1016/j.ijhydene.2024.09.378.

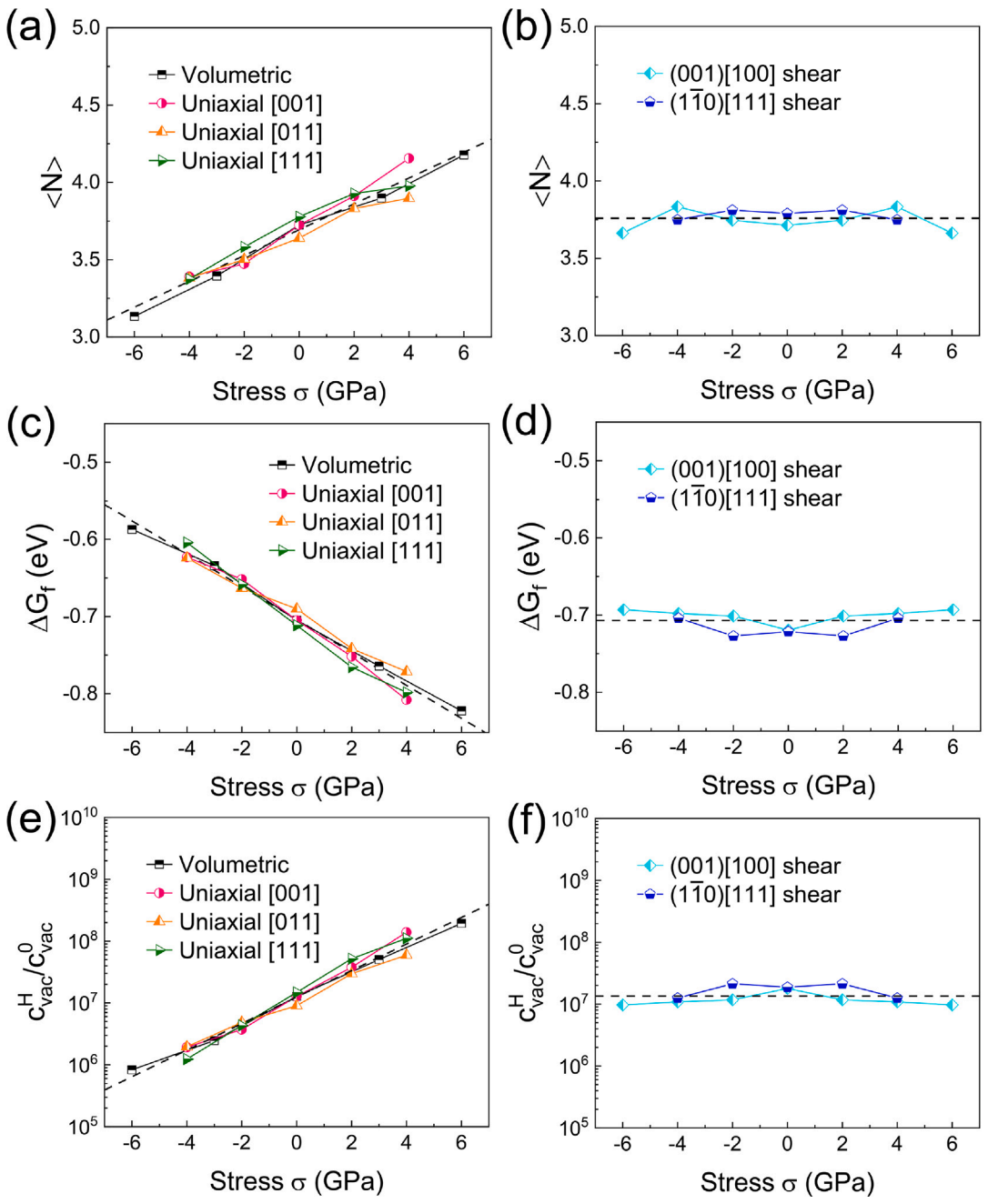

Fig. 8. (a–b) The average number $\langle N \rangle$ of hydrogen atoms trapped at monovacancy, (c–d) the formation free energy difference ΔG_f of vacancy, and (e–f) the vacancy concentration change c^H_{vac}/c^0_{vac} as a function of stress σ under various stress conditions: (a, c, e) volumetric stress, uniaxial [001], [011] and [111] stresses, and (b, d, f) (001)[100] and (1$\bar{1}$0)[111] shear stresses. The scenario is depicted with a chemical potential $\mu_{H,sol} = -2.3$ eV, corresponding to an unstressed hydrogen concentration of 2550 atomic ppm at 500 K. The dashed lines represent the linear fitting of the results.

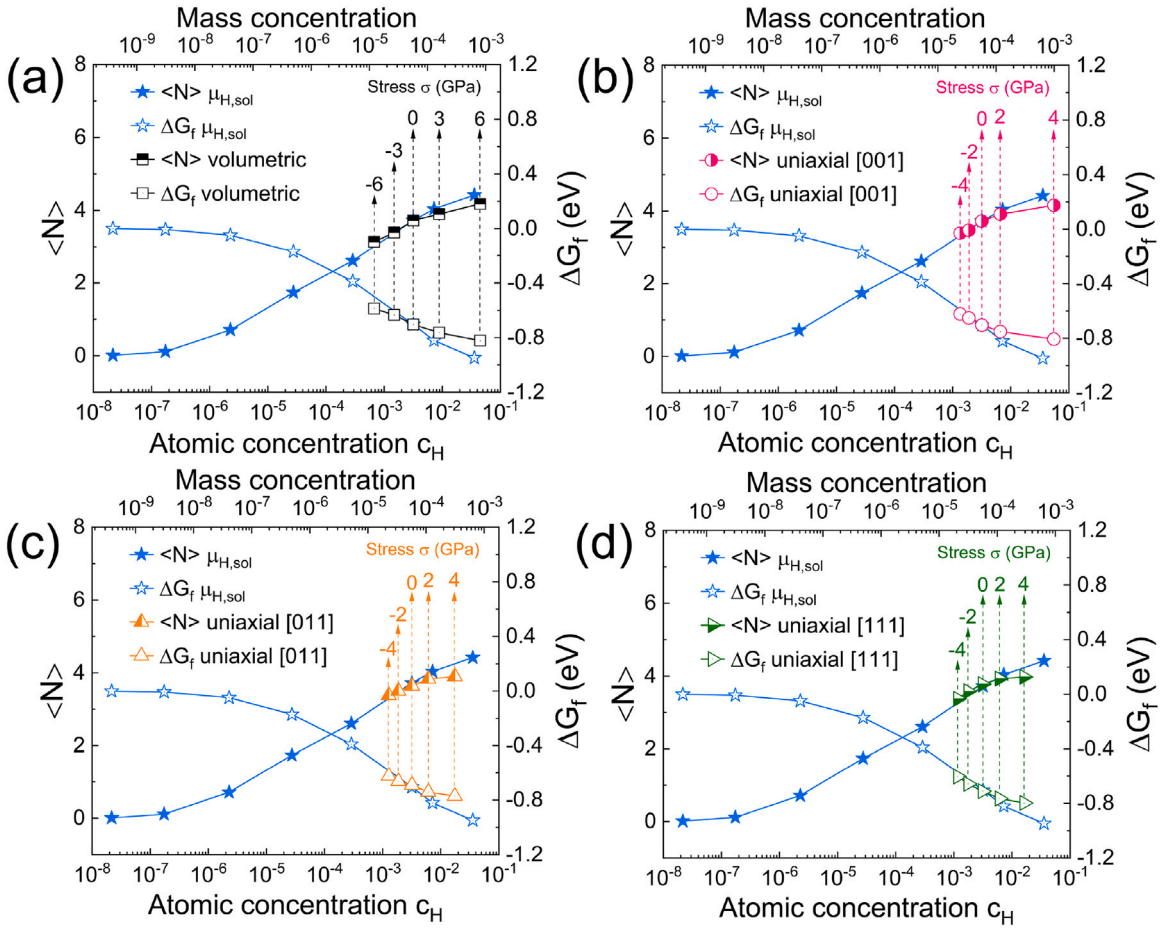

Fig. 9. The average number $\langle N \rangle$ of hydrogen atoms trapped at monovacancy and the formation free energy difference ΔG_f of vacancy as a function of hydrogen atomic concentration c_H with a variable of the external (a) volumetric stress, (b) uniaxial [001] stress, (c) uniaxial [011] stress, and (d) uniaxial [111] stress with a constant $\mu_{H,sol} = -2.3$ eV. The corresponding values of stress σ are marked. The $\langle N \rangle$ and ΔG_f, resulting from variations in the chemical potential $\mu_{H,sol}$ (ranging from −2.80 to −2.24 eV) without external stress, are plotted in all of (a)–(d) as solid and open stars for comparison. The corresponding mass concentrations of hydrogen are also shown.

References

[1] Zhang H, Fu Y, Nguyen HT, Fox B, Lee JH, Lau AK-T, Zheng H, Lin H, Ma T, Jia B. Material challenges in green hydrogen ecosystem. Coord Chem Rev 2023;494:215272.

[2] Ishaq H, Dincer I, Crawford C. A review on hydrogen production and utilization: Challenges and opportunities. Int J Hydrog Energy 2022;47(62):26238–64.

[3] Najjar YS. Hydrogen safety: The road toward green technology. Int J Hydrog Energy 2013;38(25):10716–28.

[4] Cotterill P. The hydrogen embrittlement of metals. Prog Mater Sci 1961;9(4):205–301.

[5] Oriani R. Hydrogen embrittlement of steels. Annu Rev Mater Sci 1978;8(1):327–57.

[6] Djukic MB, Bakic GM, Zeravcic VS, Sedmak A, Rajicic B. The synergistic action and interplay of hydrogen embrittlement mechanisms in steels and iron: Localized plasticity and decohesion. Eng Fract Mech 2019;216:106528.

[7] Song J, Curtin W. Atomic mechanism and prediction of hydrogen embrittlement in iron. Nat Mater 2013;12(2):145–51.

[8] Zhang S, Meng F, Fu R, Ogata S. Highly efficient and transferable interatomic potentials for α-iron and α-iron/hydrogen binary systems using deep neural networks. Comput Mater Sci 2024;235:112843.

[9] Sieverts A. Absorption of gases by metals. Z Metall 1929;21:37–46.

[10] Sugimoto H, Fukai Y. Hydrogen-induced superabundant vacancy formation in bcc Fe: Monte Carlo simulation. Acta Mater 2014;67:418–29.

[11] Nagumo M, Takai K. The predominant role of strain-induced vacancies in hydrogen embrittlement of steels: Overview. Acta Mater 2019;165:722–33.

[12] Polfus JM, Lø vvik OM, Bredesen R, Peters T. Hydrogen induced vacancy clustering and void formation mechanisms at grain boundaries in palladium. Acta Mater 2020;195:708–19.

[13] Drexler A, Konert F, Sobol O, Rhode M, Domitner J, Sommitsch C, Böllinghaus T. Enhanced gaseous hydrogen solubility in ferritic and martensitic steels at low temperatures. Int J Hydrog Energy 2022;47(93):39639–53.

[14] Kiuchi K, McLellan R. The solubility and diffusivity of hydrogen in well-annealed and deformed iron. In: Perspectives in hydrogen in metals. Elsevier; 1986, p. 29–52.

[15] Kan B, Yang Z, Li J. Characterization of a surface hydrogen charging product affecting the mechanical properties in 2205 duplex stainless steel. Materials 2019;12(10):1682.

[16] Zheng J, Liu X, Xu P, Liu P, Zhao Y, Yang J. Development of high pressure gaseous hydrogen storage technologies. Int J Hydrog Energy 2012;37(1):1048–57.

[17] Meng F-S, Du J-P, Shinzato S, Mori H, Yu P, Matsubara K, Ishikawa N, Ogata S. General-purpose neural network interatomic potential for the α-iron and hydrogen binary system: toward atomic-scale understanding of hydrogen embrittlement. Phys Rev Mater 2021;5(11):113606.

[18] Frenkel D, Smit B. Understanding molecular simulation: from algorithms to applications. Academic Press San Diego; 2002.

[19] Plimpton S. Fast parallel algorithms for short-range molecular dynamics. J Comput Phys 1995;117(1):1–19.

[20] San Marchi C, Somerday BP, Robinson SL. Permeability, solubility and diffusivity of hydrogen isotopes in stainless steels at high gas pressures. Int J Hydrog Energy 2007;32(1):100–16.

[21] Shaw HR, Wones DR. Fugacity coefficients for hydrogen gas between o degrees and 1000 degrees C, for pressures to 3000 atm. Am J Sci 1964;262(7):918–29.

[22] Puibasset J. Grand potential, Helmholtz free energy, and entropy calculation in heterogeneous cylindrical pores by the grand canonical Monte Carlo simulation method. J Phys Chem B 2005;109(1):480–7.

[23] Glensk A, Grabowski B, Hickel T, Neugebauer J. Breakdown of the arrhenius law in describing vacancy formation energies: The importance of local anharmonicity revealed by ab initio thermodynamics. Phys Rev X 2014;4(1):011018.

[24] Mendelev MI, Mishin Y. Molecular dynamics study of self-diffusion in bcc Fe. Phys Rev B 2009;80(14):144111.

[25] Chenoweth D. Gas-transfer analysis. Section h-real gas results via the van der waals equation of state and virial expansion extension of its limiting abel-noble form. Tech Rep, Sandia National Lab.(SNL-NM), Albuquerque, NM (United States); 1983.

[26] Zong H, Wiebe H, Ackland GJ. Understanding high pressure molecular hydrogen with a hierarchical machine-learned potential. Nat Commun 2020;11(1):5014.
[27] Da Silva J, Mclellan RB. The solubility of hydrogen in super-pure-iron single crystals. J Less Common Metals 1976;50(1):1–5.
[28] Hirth JP. Effects of hydrogen on the properties of iron and steel. Metall Trans A 1980;11:861–90.
[29] JO'M B, Subramanyan P. A thermodynamic analysis of hydrogen in metals in the presence of an applied stress field. Acta Metall 1971;19(11):1205–8.
[30] Kumnick A, Johnson H. Deep trapping states for hydrogen in deformed iron. Acta Metall 1980;28(1):33–9.
[31] Wagenblast H, Wriedt H. Dilation of alpha iron by dissolved hydrogen at 450° to 800°C. Metall Trans 1971;2:1393–7.
[32] Badding J, Hemley R, Mao H. High-pressure chemistry of hydrogen in metals: In situ study of iron hydride. Science 1991;253(5018):421–4.
[33] Yamakata M, Yagi T, Utsumi W, Fukai Y. In situ X-ray observation of iron hydride under high pressure and high temperature. Proc Japan Acad, Ser B 1992;68(10):172–6.
[34] Voigt W. Lehrbuch der kristallphysik:(mit ausschluss der kristalloptik), vol. 34. BG Teubner; 1910.
[35] Wriedt H, Oriani RA. Effect of tensile and compressive elastic stress on equilibrium hydrogen solubility in a solid. Acta Metall 1970;18(7):753–60.
[36] Van Leeuwen H. The kinetics of hydrogen embrittlement: a quantitative diffusion model. Eng Fract Mech 1974;6(1):141–61.
[37] Wan F, Zhan Q, Long Y, Yang S, Zhang G, Du Y, Jiao Z, Ohnuki S. The behavior of vacancy-type dislocation loops under electron irradiation in iron. J Nucl Mater 2014;455(1–3):253–7.
[38] Peng Q, Meng F, Yang Y, Lu C, Deng H, Wang L, De S, Gao F. Shockwave generates <100> dislocation loops in bcc iron. Nat Commun 2018;9(1):1–6.
[39] Arakawa K, Amino T, Mori H. Direct observation of the coalescence process between nanoscale dislocation loops with different Burgers vectors. Acta Mater 2011;59(1):141–5.
[40] Gao N, Yao Z, Lu G, Deng H, Gao F. Mechanisms for <100> interstitial dislocation loops to diffuse in BCC iron. Nat Commun 2021;12(1):225.
[41] Ramasubramaniam A, Itakura M, Carter EA. Interatomic potentials for hydrogen in α-iron based on density functional theory. Phys Rev B 2009;79(17):174101.
[42] Itakura M, Kaburaki H, Yamaguchi M. First-principles study on the mobility of screw dislocations in bcc iron. Acta Mater 2012;60(9):3698–710.
[43] Ersland C, Vatne I, Thaulow C. Atomistic modeling of penny-shaped and through-thickness cracks in bcc iron. Modelling Simul Mater Sci Eng 2012;20(7):075004.
[44] Suzudo T, Ebihara K, Tsuru T. Brittle-fracture simulations of curved cleavage cracks in α-iron: A molecular dynamics study. AIP Adv 2020;10(11).
[45] Matsumoto R, Inoue Y, Taketomi S, Miyazaki N. Influence of shear strain on the hydrogen trapped in bcc-Fe: A first-principles-based study. Scr Mater 2009;60(7):555–8.
[46] Psiachos D. Ab initio parametrized model of strain-dependent solubility of H in α-iron. Modelling Simul Mater Sci Eng 2012;20(3):035011.